OPEN ACCESS
IOP Publishing
Journal of Physics B: Atomic, Molecular and Optical Physics
J. Phys. B: At. Mol. Opt. Phys. **57** (2024) 145602 (10pp)
https://doi.org/10.1088/1361-6455/ad53af

Ultrafast x-ray scattering and electronic coherence at avoided crossings: complete isotropic signals

Eirik M Liane, Mats Simmermacher* and Adam Kirrander*

Physical and Theoretical Chemistry Laboratory, Department of Chemistry, University of Oxford, South Parks Road, Oxford OX1 3QZ, United Kingdom

E-mail: mats.simmermacher@chem.ox.ac.uk and adam.kirrander@chem.ox.ac.uk

Received 22 February 2024, revised 18 April 2024
Accepted for publication 3 June 2024
Published 18 June 2024

Abstract

Nonadiabatic transitions at conical intersections and avoided crossings play a pivotal role in shaping the outcomes of photochemical reactions. Using the photodissociation of LiF as a model, this theoretical study explores the application of gas phase nonresonant ultrafast x-ray scattering to map nonadiabatic transitions at an avoided crossing, utilizing the part of the scattering signal that probes electronic coherence directly. The presented scattering signals are rotationally averaged and calculated from two- rather than one-electron (transition) densities, which inherently accounts for all possible electronic transitions driven by the x-ray photon. This approach provides quantitative predictions of the experimental signals, thereby facilitating future experimental endeavors to observe nonadiabatic effects and coherent electron dynamics with ultrafast x-ray scattering.

Supplementary material for this article is available online

Keywords: electronic coherence, nonadiabatic transitions, photodissociation, ultrafast x-ray scattering, x-ray free-electron lasers

1. Introduction

The emergence of x-ray free-electron lasers (XFELs) has transformed ultrafast science by providing extremely bright and short x-ray pulses. One notable experimental technique enabled by XFELs is ultrafast x-ray scattering (UXS) of isolated molecules in the gas phase [1–4]. Following the first proof-of-principle experiments, [5–9] UXS has evolved rapidly. A short list of achievements includes observation of molecular alignment [7, 10–12], tracking of nuclear dynamics during photochemical reactions [6, 13–17], determination of the nuclear geometry of an electronically excited state [18, 19], detection of ionisation and charge states [13, 16], and measurement of the rearrangement of electrons in electronically excited states [19, 20]. It has also been demonstrated how to usefully combine data from UXS and complementary techniques such as time-resolved photoelectron spectroscopy [19, 21, 22]. The experimental advances have been accompanied, and often preceded, by significant theoretical work [23–46] and the development of computational tools to support the analysis and interpretation of the experiments [12, 47–53].

Extrapolating these advances, it is likely that UXS will extend into the attosecond domain in coming years. Recent upgrades of XFELs, such as LCLS-II, have significantly increased the repetition rate, which should translate into improved signal-to-noise ratio and sufficient sensitivity to

* Authors to whom any correspondence should be addressed.

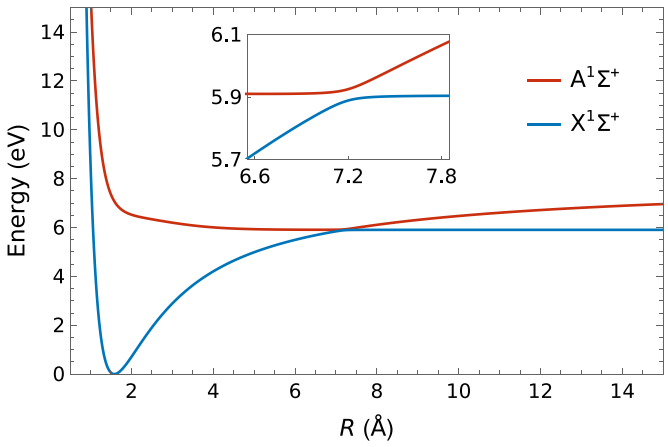

Figure 1. Adiabatic potential energy curves of the two energetically lowest-lying electronic states of LiF, $X^1\Sigma^+$ and $A^1\Sigma^+$, plotted as functions of the internuclear distance R. The electronic states are calculated at the MR-CISD/SA-CASSCF(6,12)/aug-cc-pVQZ level of theory. The inlay shows a close-up of the avoided crossing region, with the crossing located at $R_X \approx 7.19$ Å.

detect weaker effects. Crucially, the preparation of pulses with sub-femtosecond (fs) duration has already been achieved in the soft x-ray regime [54–60] and sub-fs pulses in the hard x-ray regime will follow. Combining these advances with appropriate timing and detection schemes makes attosecond time-resolved UXS experiments a realistic and timely proposition.

The enthusiasm for attosecond science across chemistry and physics [61–63], reflected by the 2023 Nobel Prize in Physics [64], stems from the role of the attosecond as the fundamental unit of time for electron dynamics, making this the next frontier in the campaign to map the dynamics of matter. In UXS, electron dynamics manifests as an interference effect alongside the normal elastic and inelastic components of the scattering signal [65]. It relies on the presence of coherence between different populated electronic states in the system and is therefore sometimes referred to as coherent mixed scattering (CMS) [37]. It is worth noting that the manner in which coherences manifest in UXS has interesting analogies in photoelectron spectroscopy [66–68].

In photoinduced dynamics, initial coherence is immediately established by the pump laser. As the system undergoes further dynamics, transient electronic coherences can appear when a molecule goes through internal conversion via conical intersections [69] or avoided crossings [70], as long as the system fulfills appropriate symmetry criteria [71]. An exciting prospect for the observation of CMS is therefore that it carries the potential to map the passage of molecules through conical intersections [69], a ubiquitous and important process in photochemistry [72]. In principle, UXS could achieve this in conjunction with the characterisation of nuclear dynamics, providing a complete measurement of photochemical dynamics.

In this paper, we demonstrate the ability of UXS to monitor non-adiabatic transitions using quantitative calculations for the molecule LiF. Figure 1 shows the electronic ground, $X^1\Sigma^+$, and first excited, $A^1\Sigma^+$, states of LiF. The excited A state supports vibrational resonances which dissociate via an avoided crossing to the ground state, while at large internuclear distances the excited state acquires ion-pair character (Li^+F^-). Due to the long-range Coulomb interaction, the resonances form a *vibrational* Rydberg series [73] and are thus also referred to as heavy Rydberg states [74–76].

Alkalihalides such as LiF and NaI have interesting properties and have consequently received extensive attention from experiments and theory over the years. Early developments in time-resolved spectroscopy exploited NaI as a model system [77, 78], finding that the lifetime of the excited wavepacket exhibited a strong dependence on the wavelength of the pump laser. This, in turn, stimulated theoretical work, which confirmed that the lifetimes in alkalihalides are highly variable due to interferometric effects [79–82]. Recent theoretical work has focussed on the quantum dynamics of the photodissociation of LiF [83, 84], demonstrating how these interference effects lead to intriguing reversals in the Fano asymmetry parameter in the spectrum [85, 86] and a powerlaw decay in the photodissociation [87]. Alkalihalides have also been used to demonstrate new theoretical non-adiabatic approximations [88] and novel control schemes [89–91].

Kowalewski *et al* have previously used the alkalihalide NaF to demonstrate qualitatively that UXS can probe the passage through an avoided crossing [36, 70]. Here, we extend their effort by carrying out a quantitative calculation of this process, accounting for the contributions of *all* electronic transitions to the inelastic and coherent mixed components of the scattering signal. Since recent work has indicated that unpopulated electronic states can make a significant contribution to the CMS signal, [46] it is pertinent to account for all final states, which is done in the current study by calculating the energy-integrated total and CMS signals from two-electron rather than one-electron (transition) densities. Moreover, we simulate the isotropic scattering signals that would be measured in an actual experiment. The overall goal is to quantify CMS accurately in order to support future experimental efforts aimed at observing electron dynamics by non-resonant scattering.

2. Theory

The quantity measured in non-resonant UXS without energy resolution is the rotationally averaged time-resolved differential x-ray scattering cross section,

$$\frac{\mathrm{d}\sigma}{\mathrm{d}\Omega} = \left(\frac{\mathrm{d}\sigma}{\mathrm{d}\Omega}\right)_{\mathrm{Th}} S(q,\tau), \tag{1}$$

where Ω is the solid angle into which a photon is scattered, $(\mathrm{d}\sigma/\mathrm{d}\Omega)_{\mathrm{Th}}$ is the differential Thomson scattering cross section of a free electron, and $S(q,\tau)$ is the isotropic scattering signal at momentum transfer q[1] and pump-probe delay time τ, [38, 65]

[1] $q = |\boldsymbol{q}|$, where $\boldsymbol{q}$ is the difference between the wave vector of the incoming and scattered photons, $\boldsymbol{q} = \boldsymbol{k}_0 - \boldsymbol{k}_s$.

$$S(q,\tau) = \mathcal{I}_\tau N_\mathrm{e} + \sum_{i,j}^{N} \int \mathcal{I}(t-\tau) \times \left\langle \chi_j(t) \right| \left\langle \Lambda_{ij}^{2\mathrm{e}}(\boldsymbol{q},\bar{\boldsymbol{R}}) \right\rangle_0 \left| \chi_i(t) \right\rangle \mathrm{d}t. \tag{2}$$

Here, $\mathcal{I}(t-\tau)$ is the photon number intensity of the x-ray probe pulse at time $t-\tau$, $\mathcal{I}_\tau$ is the integral of $\mathcal{I}(t-\tau)$ over time t equal to the total number of photons in the pulse, and N_e is the number of electrons in the target molecule. The double sum in the first line of equation (2) runs over all N populated electronic eigenstates $|\varphi_k(\bar{\boldsymbol{R}})\rangle$ of the molecular wavepacket,

$$\left|\Psi(t)\right\rangle = \sum_{k}^{N} \left|\chi_k(t)\right\rangle \left|\varphi_k(\bar{\boldsymbol{R}})\right\rangle, \tag{3}$$

prepared by the pump pulse. For a given electronic state with index k, $|\chi_k(t)\rangle$ is the corresponding vibrational wavepacket at time t. $\bar{\boldsymbol{R}} = \{\boldsymbol{R}_1, \ldots, \boldsymbol{R}_{N_\mathrm{ic}}\}$ is the set of all internal nuclear coordinates and the electronic states depend parametrically on $\bar{\boldsymbol{R}}$.

Finally, $\Lambda_{ij}^{2\mathrm{e}}(\boldsymbol{q},\bar{\boldsymbol{R}})$ in equation (2) is the two-electron scattering matrix element of the electronic states with indices i and j. It relates to the probability of scattering for a given three-dimensional momentum transfer vector $\boldsymbol{q}$ within the Waller-Hartree approximation [92] and can be calculated as the Fourier transform of the two-electron (transition) density, $\rho_{ij}(\boldsymbol{r}_1,\boldsymbol{r}_2,\bar{\boldsymbol{R}})$, from real into reciprocal space,

$$\Lambda_{ij}^{2\mathrm{e}}(\boldsymbol{q},\bar{\boldsymbol{R}}) = 2 \iint \mathrm{e}^{\imath \boldsymbol{q}\cdot(\boldsymbol{r}_2-\boldsymbol{r}_1)} \rho_{ij}(\boldsymbol{r}_1,\boldsymbol{r}_2,\bar{\boldsymbol{R}})\, \mathrm{d}\boldsymbol{r}_1 \mathrm{d}\boldsymbol{r}_2, \tag{4}$$

with the imaginary unit $\imath$ and electronic coordinates $\boldsymbol{r}_1$ and $\boldsymbol{r}_2$. Moreover, the brackets $\langle \ldots \rangle_0$ around the scattering matrix element $\Lambda_{ij}^{2\mathrm{e}}(\boldsymbol{q},\bar{\boldsymbol{R}})$ in equation (2) imply rotational averaging for completely unaligned molecules in a thermal ensemble. The subscript 0 refers to the order of the spherical Bessel function l that follows from rotationally averaging of the exponential $\exp\left[\imath \boldsymbol{q}\cdot(\boldsymbol{r}_2-\boldsymbol{r}_1)\right]$ in equation (4) [65]. For an isotropic ensemble, the exponential reduces to a zeroth-order spherical Bessel function, i.e. a sinc function, also known as the Debye kernel, [93–97]

$$\left\langle \Lambda_{ij}^{2\mathrm{e}}(\boldsymbol{q},\bar{\boldsymbol{R}}) \right\rangle_0 = 2 \iint \mathrm{sinc}\big(q\,(r_2-r_1)\big) \rho_{ij}(\boldsymbol{r}_1,\boldsymbol{r}_2,\bar{\boldsymbol{R}})\, \mathrm{d}\boldsymbol{r}_1 \mathrm{d}\boldsymbol{r}_2. \tag{5}$$

We note that the pump pulse will make the sample slightly anisotropic due to preferential excitation along its polarisation vector. This leads to higher-order contributions to the scattering signal, most notably with $l=2$ [10, 39]. These anisotropic contributions, however, are usually much weaker than the isotropic component unless additional laser-driven alignment [7, 11, 98] is applied. We will therefore only consider isotropic scattering signals and leave the discussion of the more subtle effect of anisotropy for future work.

The scattering signal in equation (2) can be split into three physically distinct components,

$$S(q,\tau) = S_\mathrm{bg} + S_\mathrm{ex}(q,\tau) + S_\mathrm{cm}(q,\tau). \tag{6}$$

The first component is a structure- and time-independent background signal,

$$S_\mathrm{bg} = \mathcal{I}_\tau N_\mathrm{e}, \tag{7}$$

proportional to the scattering from N_e free electrons. The second component is the excess scattering,

$$S_\mathrm{ex}(q,\tau) = \sum_{i}^{N} \int \mathcal{I}(t-\tau) \times \left\langle \chi_i(t) \right| \left\langle \Lambda_{ii}^{2\mathrm{e}}(\boldsymbol{q},\bar{\boldsymbol{R}}) \right\rangle_0 \left| \chi_i(t) \right\rangle \mathrm{d}t, \tag{8}$$

which contains the diagonal elements, $i=j$, of equation (2). The background and excess scattering combined equal the sum of the elastic and inelastic scattering, which is also known as total scattering. Detection without energy resolution neither allows for separation of the elastic and inelastic components, nor for a restriction of the inelastic transitions that contribute to the signal.

The third and final component is the previously mentioned CMS,

$$S_\mathrm{cm}(q,\tau) = 2 \sum_{i}^{N-1} \sum_{j>i}^{N} \int \mathcal{I}(t-\tau) \times \mathrm{Re}\left[\left\langle \chi_j(t) \right| \left\langle \Lambda_{ij}^{2\mathrm{e}}(\boldsymbol{q},\bar{\boldsymbol{R}}) \right\rangle_0 \left| \chi_i(t) \right\rangle \right] \mathrm{d}t, \tag{9}$$

which contains the off-diagonal elements, $i \neq j$, from equation (2). A comparison of equations (8) and (9) reveals the difference between excess scattering and CMS. While excess scattering effectively probes the population of the electronic states, $\langle \chi_i(t)|\chi_i(t)\rangle$, CMS probes the coherence between electronic states, $\langle \chi_j(t)|\chi_i(t)\rangle$, which is a prerequisite for the presence of coherent electron dynamics in the molecule. We note that the precise distinction between CMS and total scattering is somewhat arbitrary when the electronic states are non-adiabatically coupled. The distinction of both components then depends on the representation, i.e. whether the states are, for instance, adiabatic or diabatic. It is only the complete signal, the sum of coherent mixed and total scattering, that is invariant under change of representation.

Alternatively, the scattering signal in equation (2) can also be expressed as,

$$S(q,\tau) = \sum_{i,j}^{N} \sum_{f}^{\infty} \int \mathcal{I}(t-\tau) \times \left\langle \chi_j(t) \right| \left\langle L_{fj}^{*}(\boldsymbol{q},\bar{\boldsymbol{R}})\, L_{fi}(\boldsymbol{q},\bar{\boldsymbol{R}}) \right\rangle_0 \left| \chi_i(t) \right\rangle \mathrm{d}t, \tag{10}$$

where the sum over f runs over *all* energetically accessible final states that can be excited by inelastic scattering of an x-ray photon. Note that, due to the high mean-photon energy of the x-ray probe pulse, the sum over f is infinite, while the sums over i and j are not since they refer to the electronic states populated by the pump pulse. The scattering signal is now defined via one-electron scattering matrix elements $L_{fi}(\boldsymbol{q},\bar{\boldsymbol{R}})$. Similarly to the two-electron scattering matrix element $\Lambda_{ij}^{2\mathrm{e}}(\boldsymbol{q},\bar{\boldsymbol{R}})$ defined

in equation (4) above, $L_{fi}(\boldsymbol{q},\bar{\boldsymbol{R}})$ can be calculated by a Fourier transform from real into reciprocal space. However, in this instance it is the one-electron (transition) density, $\rho_{fi}(\boldsymbol{r},\bar{\boldsymbol{R}})$, that is Fourier transformed,

$$L_{fi}(\boldsymbol{q},\bar{\boldsymbol{R}}) = \int \mathrm{e}^{\mathrm{i}\boldsymbol{q}\cdot\boldsymbol{r}}\, \rho_{fi}(\boldsymbol{r},\bar{\boldsymbol{R}})\, \mathrm{d}\boldsymbol{r}. \tag{11}$$

Again, rotational averaging of an isotropic ensemble in equation (10) reduces the exponential to a sinc function,

$$\left\langle L^{*}_{fj}(\boldsymbol{q},\bar{\boldsymbol{R}}) L_{fi}(\boldsymbol{q},\bar{\boldsymbol{R}}) \right\rangle_{0} = \iint \mathrm{sinc}\big(q\,(r_2 - r_1)\big)\, \rho^{*}_{fj}(\boldsymbol{r}_1,\bar{\boldsymbol{R}}) \times \rho_{fi}(\boldsymbol{r}_2,\bar{\boldsymbol{R}})\, \mathrm{d}\boldsymbol{r}_1 \mathrm{d}\boldsymbol{r}_2. \tag{12}$$

Note that rotational averaging always applies to scattering probabilites, not the individual amplitudes. Equation (12) therefore contains a product of two one-electron scattering matrix elements.

The coherent mixed component of the scattering signal in equation (10) is then given by the sum of all off-diagonal elements, $i \neq j$, analogous to equation (9),

$$S_{\mathrm{cm}}(q,\tau) = 2 \sum_{i}^{N-1} \sum_{j>i}^{N} \sum_{f}^{\infty} \int \mathcal{I}(t-\tau) \times \mathrm{Re}\left[\left\langle \chi_j(t) \right| \left\langle L^{*}_{fj}(\boldsymbol{q},\bar{\boldsymbol{R}}) \times L_{fi}(\boldsymbol{q},\bar{\boldsymbol{R}}) \right\rangle_{0} \left| \chi_i(t) \right\rangle \right] \mathrm{d}t. \tag{13}$$

While equations (10) and (2), as well as equations (9) and (13), are formally equivalent, it is important to note that equation (10) involves an infinite sum over all final states. This sum also includes the continuum of singly ionised states and is not guaranteed to converge when only the energetically lowest-lying electronic states are considered [46]. A truncation of equation (10) can therefore lead to incomplete or, in the case of CMS, even spurious results.

The most severe truncation possible only considers the N electronic states with non-zero population and has been applied in a number of seminal *proof-of-concept* studies (see, for instance, [44, 69, 70]). We will from here on refer to this truncation as the *fewest-states approximation* (FSA). For a first qualitative investigation of CMS, the FSA was certainly a well justified starting point. Future studies of UXS without energy resolution should, however, carefully benchmark the FSA against the intrinsically converged evaluation of equation (2) or refrain from using a truncated equation (10) altogether. The FSA alone does not reliably provide quantitative signals and may even lead to unrecognised errors. In this article, we will use equation (2) throughout and compare briefly with results of the FSA at the end of section 4.

3. Computational methods

The quantum dynamics in LiF is propagated along the intranuclear coordinate, R, on the electronic ground state ($\mathrm{X}^1\Sigma^+$) and the first excited state ($\mathrm{A}^1\Sigma^+$), as shown in figure 1. The potential energy curves and derivative non-adiabatic coupling matrix elements (NACMEs) for LiF are calculated using MR-CISD/SA-CASSCF(6,12)/aug-cc-pVQZ in MOLPRO [99], which closely echoes the approach taken by Varandas [100] for the electronic structure. Details of the benchmarking are provided in the supplementary information (SI). The NACMEs are calculated by numerical differentiation via the DDR program using the three-point method.

The wavepacket is propagated within the diabatic representation by numerical integration of the time-dependent Schrödinger equation in the molecular frame using the Strang–Marchuk split operator method as implemented in WAVEPACKET [101] using Matlab [102]. The temporal step size is 0.01 fs, which ensures conservation of energy and total population. An absorbing potential is placed at nuclear separation $R \geqslant 29$ Å, and the absorbed wavepacket at each timestep is propagated classically towards larger R with a constant average velocity of $v = 0.0622$ Å fs^{-1} (see SI for details). The simulation is initialised with the molecule in its electronic and vibrational ground state, $\mathrm{X}^1\Sigma^+(\nu = 0)$, obtained by imaginary time propagation. The excitation is included explicitly, using a Gaussian ultraviolet pump pulse with a 6.8 eV mean photon energy, a 10 fs full-width half-maximum (FWHM) pulse duration, and a maximum electric field amplitude of 59.4 MV cm^{-1}. The pump excites approximately 10% of the ground state population to the first electronically excited state, $\mathrm{A}^1\Sigma^+ \longleftarrow \mathrm{X}^1\Sigma^+(\nu = 0)$.

The scattering signal is calculated via equation (2) assuming a Gaussian-shaped 10 keV x-ray probe pulse of 10 fs FWHM duration. The isotropic two-electron scattering matrix elements defined in equation (4) are calculated from *ab-initio* electronic wavefunctions, obtained by SA-CASSCF(6,23)/aug-cc-pVTZ, using methods and codes developed in our group [49, 103–106]. Given the formal equivalence of equations (2) and (10) with an untruncated sum over f, these scattering matrix elements implicitly account for all inelastic transitions from the two states populated by the pump pulse to all energetically accessible final states, bound and continuum [46]. To limit the computational effort, which scales exponentially with the size of the wavefunction, the scattering matrix elements are calculated at a lower level of electronic structure theory than the potential energy curves and NACMEs used for the dynamics. The slight discrepancy that results from a small shift in the position of the avoided crossing is adjusted for by scaling the scattering matrix elements by the calculated (transition) dipole moments. Details on this scaling are provided in the SI. Finally, the asymptotic scattering signal of the dissociated portion of the wavepacket is calculated using the independent atom model [107, 108].

In the results section, the scattering signals are given as a percent difference signal,

$$\%\Delta S_{\kappa}(q,\tau) = 100 \times \frac{S_{\kappa}(q,\tau) - S_{\kappa}(q,-\infty)}{S(q,-\infty)}, \tag{14}$$

where $S_{\kappa}(q,\tau)$ is a component of the scattering signal (either total or CMS) at pump-probe delay time τ and $S(q,-\infty)$ is the sum of all components according to equation (6) before

the arrival of the pump pulse, corresponding to the so-called 'pump-off' signal.

4. Results

4.1. Vibronic wave packet

The dynamics of the excited nuclear wavepacket is shown in figure 2. After excitation by the pump pulse centered at $t = 0$ fs, the excited wavepacket evolves on the first electronically excited state towards the avoided crossing at $R_X \approx 7.19$ Å. At the avoided crossing, a large fraction of the wavepacket transitions non-adiabatically to the ground state. This can be seen in figure 3 by the strong decrease in the excited state population, $P_2(t) = \langle\chi_2(t)|\chi_2(t)\rangle$, at $t \approx 108$ fs. Figure 2 further shows that the dissociated part of the wavepacket that transitioned to the ground state proceeds with a constant average velocity towards larger interatomic distances. The bound component that remains on the excited state decelerates as it approaches the outer turning point on the excited state potential. After that, it passes the avoided crossing a second and a third time, marked by a decrease and a subsequent increase of the excited state population between 500 and 1000 fs. The excited wavepacket also displays significant dispersion, seen by the broadening of the wavepacket over time. After the third pass over the avoided crossing, the excited wavepacket is sufficiently dispersed for further decay to occur without any significant structure.

Figure 3 also shows the square root of the degree of electronic coherence, $\sqrt{\mathcal{M}_{\text{coh}}(t)} = \sqrt{2}\,\big|\langle\chi_1(t)|\chi_2(t)\rangle\big|$, which maps onto the integrated absolute value of the CMS signal [37]. The value of $\sqrt{\mathcal{M}_{\text{coh}}(t)}$ is strongly peaked around $t = 3$ fs with a maximum value of 0.256, which reflects the coherent excitation of the molecule by the pump pulse. There is a second sharp, almost Gaussian-shaped peak around $t \approx 108$ fs with a maximum value of $\sqrt{\mathcal{M}_{\text{coh}}} \approx 0.033$. This peak corresponds to the first passing through the avoided crossing and is significantly weaker than the first peak because less amplitude is transferred between states. The short-lived nature of the peak is due to the de-phasing that happens as the two parts of the wavepacket move away from the avoided crossing. Between 600 and 1200 fs, $\sqrt{\mathcal{M}_{\text{coh}}}$ increases again, in large part due to the return of the excited state wavepacket to the Franck–Condon region and the associated revival of overlap with the depleted ground-state wavepacket. Additionally, some coherence is created by non-adiabatic transitions during the second and third passing through the avoided crossing, but this contribution is relatively small due to the dispersion of the wavepacket and weak population transfer.

4.2. UXS signals

The total and CMS signals of the simulated wavepacket are shown in figures 4(A) and (B), respectively. After excitation, the total difference scattering signal displays a negative band at low values of q and a positive band between $q = 2$ and $q = 4$, which reflects the increasing distance between the atoms in

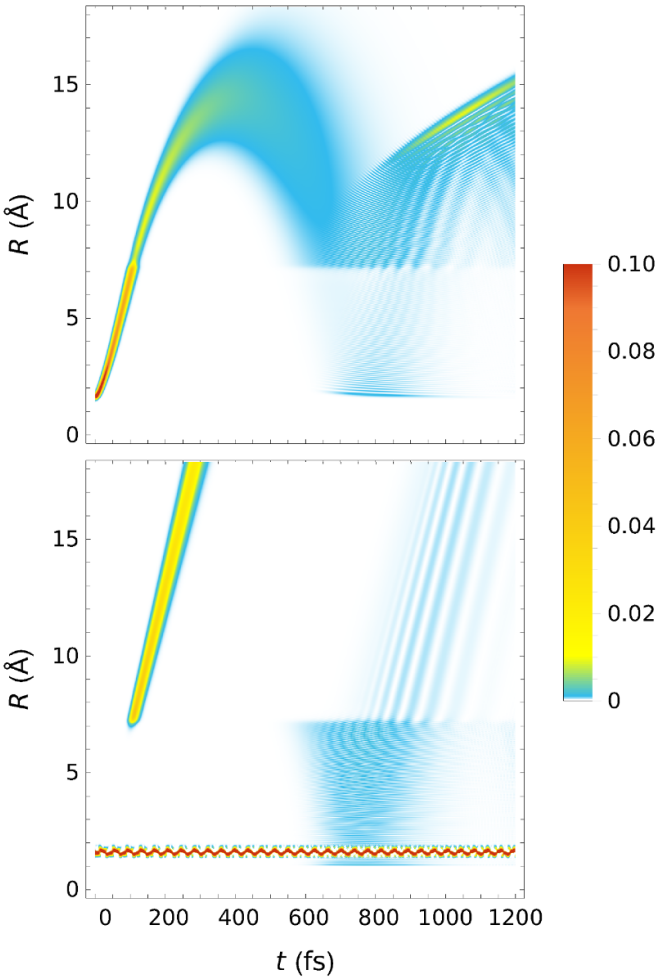

Figure 2. Nuclear densities for LiF upon excitation by a UV pulse with 10 fs duration, $A^1\Sigma^+ \leftarrow X^1\Sigma^+(\nu = 0)$, as function of time t and internuclear distance R. *Top*: The first electronically excited state, $A^1\Sigma^+$, $|\chi_2(R,t)|^2$. *Bottom*: The electronic ground state, $X^1\Sigma^+$, $|\chi_1(R,t)|^2$. *Note*: In the ground state plot we have subtracted $-0.85\ |\chi_1(R,-\infty)|^2$ to help visualize the oscillations in the ground state density in the Franck–Condon region.

the dissociating molecule. The dissociation is also responsible for the ripple effect in the negative band. On top of this, there is an imprint of a fast oscillation with a period $T \approx 46$ fs, corresponding to the oscillation of the depleted ground state wavepacket seen in the bottom of figure 2. These oscillations originate from the cycling of the wavepacket back onto the electronic ground state during the excitation process, leading to the population of higher-lying vibrational energy levels on the electronic ground state. The time-scale is therefore roughly related to the energy gap between the ground and first-excited vibrational state on the electronic ground state at the equilibrium geometry, which corresponds to a period $T \approx 38$ fs.

The CMS signal has a single peak at $\tau \approx 108$ fs, which arises from the first non-adiabatic transition through the avoided crossing. This demonstrates the capability of CMS to probe transient electronic coherences [37, 70]. The signal is relatively weak, however, peaking at a percent difference of only 0.06%. Given that the highest experimental

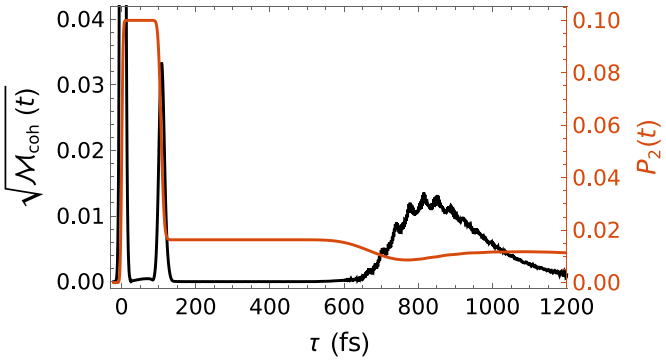

Figure 3. The population of the first electronically excited state of LiF, $P_2(t)$, and the square root of the degree of electronic coherence, $\sqrt{\mathcal{M}_{\mathrm{coh}}(t)}$, as functions of time t. The pump pulse is centred at $t = 0$.

accuracy demonstrated so far has been on the order of 0.1%, [20] the experimental detection of the coherent mixed signal in figure 4(B) would pose a significant challenge. This could potentially be overcome at LCLS-II thanks to the much higher repetition rate on offer, which is anticipated to significantly improve signal-to-noise [3, 105]. One may also consider possible routes for increasing the strength of the CMS signal to facilitate experimental observation. Potential strategies include focusing of the wavepacket to increase the degree of coherence [109, 110] or amplifying the electronic coherence by resonant infrared pulses [111]. In addition, the utilization of twisted x-rays to isolate the CMS signal has been suggested by Mukamel and coworkers [112].

Interestingly, the strong immediate electronic coherence established by the pump pulse around $\tau \approx 3$ fs and its revival after $\tau \approx 600$ fs is not visible in the isotropic scattering signals in figure 4. This can be explained as follows: resonant one-photon excitation prepares a rotational wavepacket on the electronically excited state that is proportional to $\cos\beta$, where β is the angle between the polarisation vector of the pump laser and the transition dipole moment of the molecule [65, 97]. The rotational transition density between the wavepacket on the electronically excited state and the isotropic thermal ensemble on the electronic ground state is therefore also proportional to $\cos\beta$, which does not project onto $l = 0$ or $l = 2$. The isotropic CMS signal must therefore vanish at $\tau \approx 3$ fs and after $\tau \approx 600$ fs. To resolve the electronic coherence directly established by the pump pulse, one must either pump the system via two-photon absorption or orient the molecule in its electronic ground state before it is excited and potentially employ energy resolving detectors. The latter was at least implicitly assumed in, for instance, [27, 28, 35, 37, 40, 43].

At the avoided crossing however, the amplitude transferred from the electronically excited state back to the electronic ground state is proportional to $\cos\beta$ as well. The resulting transition density is therefore aligned according to $\cos^2\beta$, which gives rise to the non-vanishing isotropic component of the CMS signal at $\tau \approx 108$ fs. (The smaller anisotropic component with $l = 2$ that follows from $\cos^2\beta$ is not considered here.)

Moreover, the electronic coherence established directly by the pump pulse oscillates rapidly with a period defined by the mean photon energy of the laser, i.e. $T = h/(6.8\ \mathrm{eV}) \approx 0.61$ fs. With a 10-fs duration x-ray probe pulse, the respective CMS signal must vanish regardless of rotational averaging. At the avoided crossing, in contrast, the electronic coherence established by the non-adiabatic transfer of amplitude oscillates with a two orders of magnitude longer period. Here, the characteristic period is determined by the energy difference between the two electronic states in the region of strong non-adiabatic coupling around $R = R_{\mathrm{X}}$. Considering the range of internuclear distances where the non-adiabatic coupling amounts to at least 20% of its maximum value, i.e. 6.92–7.44 Å, the potential energy curves of both states differ by values in the range 0.036–0.090 eV, which implies a period in the range of 46–114 fs. This is longer than the 17.3 fs FWHM of $\sqrt{\mathcal{M}_{\mathrm{coh}}}$ at $\tau \approx 108$ fs and well above the assumed 10-fs duration of the x-ray probe pulse. The CMS signal at the avoided crossing can therefore be resolved.

4.3. Comparison to previous work on NaF

We can now compare the UXS signals in figure 4 with the aforementioned and closely related results published by Kowalewski *et al* [36, 70]. These results comprise elastic, inelastic, and coherent mixed x-ray scattering signals for perfectly aligned sodium fluoride; a molecule qualitatively very similar to the lithium fluoride employed here. Thereby, Kowalewski *et al* demonstrated for the first time that UXS can be used to probe transient electronic coherences that emerge at conical intersections and avoided crossings. However, they reported scattering signals solely for the Cartesian component of the momentum transfer vector that corresponds to the molecular axis, i.e. q_x if the molecule is aligned with the laboratory x-axis. The two other Cartesian components, q_y and q_z, were both set to zero. As a first proof-of-concept simulation, they also applied the FSA, corresponding to a strong truncation of equation (10).

Current UXS experiments, in contrast, measure scattering signals as functions of the radial momentum transfer coordinate q rather than q_x. They record these signals on two-dimensional detectors, which implies that the component of $\boldsymbol{q}$ orthogonal to the detector plane, q_z, cannot be zero for $q_x > 0$ (see SI for discussion). Most experiments also start from isotropic ensembles and do not achieve perfect alignment of the molecules. Moreover, previous simulations have shown that the FSA is not always reliable [38, 46]. It is therefore imperative that the seminal simulations of Kowalewski *et al* are benchmarked against calculations that fully account for these factors.

Despite these differences and a four times shorter pulse duration, the CMS signal of Kowalewski *et al* is remarkably similar to the one shown in figure 4(B) above. In both simulations, the short-lived electronic coherence at the avoided crossing leads to a short-lived coherent mixed component of the scattering signal that is strongest at relatively low momentum transfer and contributes with the same order of magnitude to the overall scattering signal. However, all components of the scattering

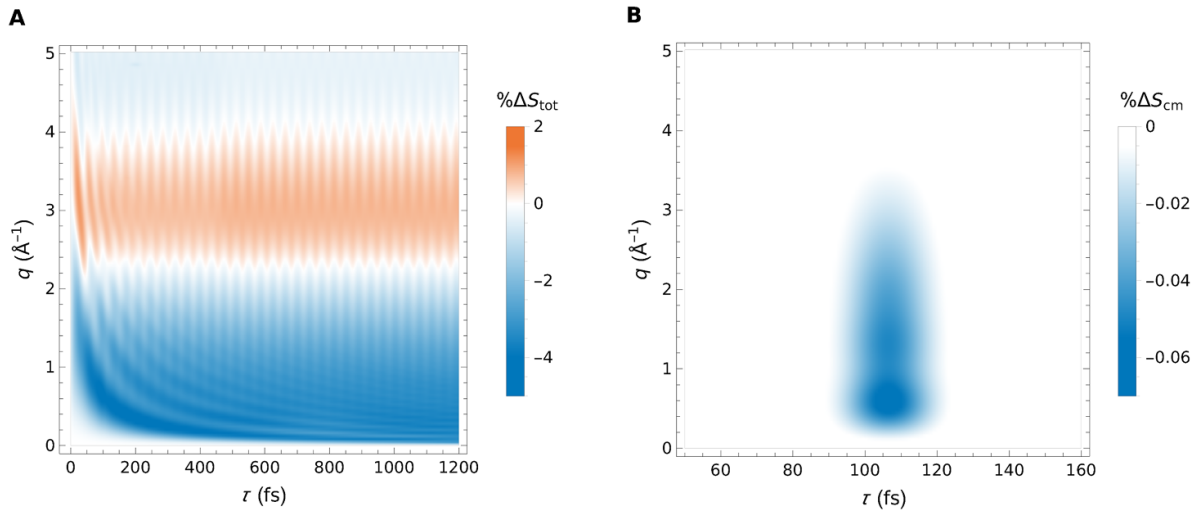

Figure 4. Plots of the total (A) and coherent mixed (B) percent-difference scattering signals of photoexcited LiF probed by a hard x-ray pulse with 10 fs duration as a function of momentum transfer q and pump-probe delay time τ. The distinction between the total and coherent mixed signals is based upon the adiabatic representation of the two non-adiabatically coupled electronic states.

signal in [70] display pronounced local maxima and minima along q_x that are not present in the isotropic signals in figure 4 above. These strong interferences are a consequence of the authors' choice of perfect alignment of the molecular axis with the laboratory x-axis and measurement in q_x-direction (see SI for detailed discussion). Rotational averaging of the UXS signal significantly dampens these features.

Moreover, the coherent mixed component in [70] undergoes a sign reversal over time. This is perhaps attributable to the real part of the electronic coherence changing sign after most of the excited state wave packet has passed through the avoided crossing. While the real part of the electronic coherence simulated in this article shows a similar sign reversal (see SI), the coherent mixed signal in figure 4(B) does not. This is likely attributable to a combination of the diminished electronic coherence following the sign reversal and the rapid decline in intensity for the off-diagonal two-electron scattering matrix elements after the avoided crossing. Furthermore, it is possible that imaginary-valued contributions that arise from the FSA for a perfectly aligned molecule interfere with the imaginary part of the electronic coherence. Such spurious interferences are absent in figure 4(B) since the isotropic two-electron scattering matrix element in equation (9) is real-valued only.

To further benchmark the performance of the FSA for the coherent mixed component, figure 5 compares the exact two-electron scattering matrix element,

$$\left\langle \Lambda_{12}^{2e}(\boldsymbol{q},R)\right\rangle_0,$$

with its counterpart in the FSA,

$$\left\langle \Lambda_{12}^{FSA}(\boldsymbol{q},R)\right\rangle_0 = \left\langle L_{12}^{*}(\boldsymbol{q},R)L_{11}(\boldsymbol{q},R)\right\rangle_0 + \left\langle L_{22}^{*}(\boldsymbol{q},R)L_{21}(\boldsymbol{q},R)\right\rangle_0.$$

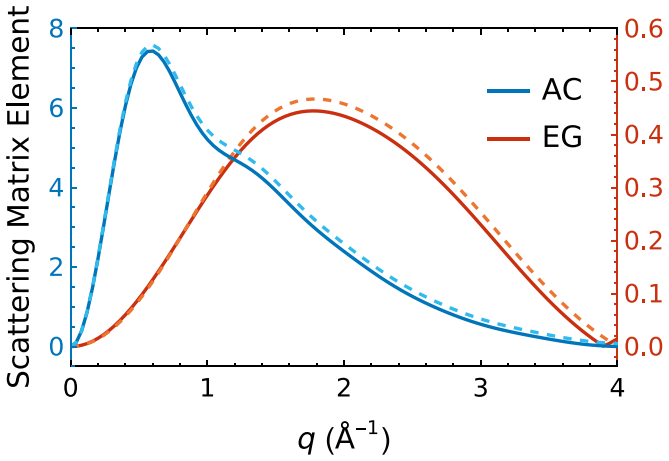

Figure 5. Absolute values of rotationally averaged scattering matrix elements in units of the Thompson scattering cross-section $(\mathrm{d}\sigma/\mathrm{d}\Omega)_{\mathrm{Th}}$ for coherent mixed scattering of LiF at the avoided crossing (AC) and in its equilibrium geometry (EG), plotted as functions of momentum transfer q. The solid lines refer to the exact two-electron scattering matrix elements and the dashed lines to their counterparts in the FSA.

In contrast to previous work that discussed significant failures of the FSA, [46] in particular for states with different inversion symmetries, the approximation works remarkably well in this case. The good performance of the FSA can partially be ascribed to the fact that both states share Σ^+ symmetry and that lithium fluoride contains more electrons than the two-electron systems considered so far (see SI for more detailed discussion). It is also possible that the error in the FSA is diminished by the rotational averaging, as the spurious imaginary valued contributions that arise in the FSA for aligned molecules cancel out.

Although figure 5 demonstrates that the FSA works well for the coherent mixed component in figure 4(B), it cannot

adequately account for the inelastic component of the total scattering signal,

$$S_{\mathrm{in}}(q,\tau) = \sum_{i}^{N}\sum_{f\neq i}^{\infty} \int \mathcal{I}(t-\tau) \times \left\langle \chi_i(t) \right| \left\langle \left| L_{fi}(\boldsymbol{q},\bar{\boldsymbol{R}}) \right|^2 \right\rangle_0 \left| \chi_i(t) \right\rangle \mathrm{d}t. \quad (15)$$

Any finite truncation of the sum over f inevitably leads to an incomplete inelastic component that deviates significantly from what one would obtain by subtracting the elastic from the total scattering signal [38, 46, 65]. We emphasise, however, that the main conclusion of [36, 70] holds beyond the limitations of their underlying assumptions and is further strengthened by this work: UXS *can* probe transient electronic coherence at avoided crossings or conical intersections.

5. Conclusion

In this paper, our calculations focused on the isotropic component of the rotationally averaged signal. It is important to recognise that real-world experiments inherently introduce some anisotropy due to the preferential excitation of molecules with transition dipole moments aligned with the polarity of the pump pulse. A natural expansion of this work is therefore to include higher order corrections to the rotational averaging, particularly the term with $l = 2$, to account for this anisotropy.

If the coherent mixed signal is particularly pronounced in the anisotropic component, its contribution could potentially be extracted from the experimental signal by means of a Legendre decomposition. Beyond such a Legendre decomposition, the identification and isolation of the CMS signal is an issue that requires careful consideration. In situations where the nuclear and electronic dynamics are only weakly coupled, a time filtering approach could be applied. However, this does not work for imaging nonadiabatic transitions, for which the time scales of the electronic and nuclear motion become indistinguishable. In this situation, the most robust way to identify the coherent mixed component is likely a detailed comparison of the experimental and simulated data. We note that this puts high demands on detector calibration, error correction, and on the signal-to-noise ratio in the experiment. In addition, it requires a highly accurate simulation of the measured scattering signal and therefore necessitates a computational approach such as the one described and utilised in this article.

The comparison between the work conducted on LiF in this study and that on NaF by Kowalewski *et al* [36, 70] highlights the importance of modelling simulations according to experimental conditions. Specifically, this entails accounting for rotational averaging and calculating the scattering signal as a function of the radial momentum transfer coordinate. Neglecting these aspects may yield a satisfactory qualitative description but is certainly insufficient to accurately predict experimental signals. Additionally, our findings demonstrate that the fewest-states approximation provides an acceptable description of CMS in LiF, contrary to previous examples where the FSA has been shown to fail [37, 46]. This demonstrates that the FSA might be acceptable under certain conditions, offering a route to reduce the computational cost of scattering calculations. However, it is imperative to thoroughly benchmark the FSA before its application, as the conditions under which the FSA remains valid are still poorly understood.

In summary, the outcomes of this study demonstrate how CMS can be used to probe nonadiabatic transitions at avoided crossings, which extends more broadly to transitions at conical intersections. The presented work is calculated taking into account the conditions of current UXS experiments, establishing the foundation for the prospective experimental observation of electron dynamics with UXS, which offers new avenues to study the fundamental processes of photochemistry and photophysics.

Data availability statement

All data that support the findings of this study are included within the article (and any supplementary files).

Acknowledgments

E M L acknowledges a PhD Studentship of the UK XFEL Physical Sciences Hub funded by the Science and Technology Facilities Council (STFC). M S and A K acknowledge funding from the Engineering and Physical Sciences Research Council (EPSRC) EP/V006819/2. A K further acknowledges funding EP/V049240/2, EP/X026698/1 and EP/X026973/1 from the EPSRC, RPG-2020-208 from the Leverhulme Trust, and support from the Department of Energy, Office of Science, Basic Energy Sciences, under Award Number DE-SC0020276.

ORCID iDs

Eirik M Liane https://orcid.org/0009-0000-9957-9195
Mats Simmermacher https://orcid.org/0000-0001-9848-7010
Adam Kirrander https://orcid.org/0000-0002-3347-8137

References

[1] Budarz J M, Minitti M P, Cofer-Shabica D V, Stankus B, Kirrander A, Hastings J B and Weber P M 2016 *J. Phys. B: At. Mol. Opt. Phys.* **49** 034001
[2] Stankus B *et al* 2020 *J. Phys. B: At. Mol. Opt. Phys.* **53** 234004
[3] Odate A, Kirrander A, Weber P M and Minitti M P 2023 *Adv. Phys.* X **8** 2126796
[4] Yong H, Kirrander A and Weber P M 2024 Time-resolved x-ray scattering of excited state structure and dynamics *Structural Dynamics With X-ray and Electron Scattering* (*Theoretical and Computational Chemistry Series* vol 25) 1st edn, ed K Amini, A Rouzée and M J J Vrakking (Royal Society of Chemistry) ch 3, p 344
[5] Minitti M P *et al* 2014 *Faraday Discuss.* **171** 81
[6] Minitti M P *et al* 2015 *Phys. Rev. Lett.* **114** 255501
[7] Küpper J *et al* 2014 *Phys. Rev. Lett.* **112** 083002
[8] Glownia J M *et al* 2016 *Phys. Rev. Lett.* **117** 153003

[9] Bennett K, Kowalewski M and Mukamel S 2017 *Phys. Rev. Lett.* **119** 069301
[10] Yong H *et al* 2018 *J. Phys. Chem. Lett.* **9** 6556–62
[11] Kierspel T *et al* 2020 *J. Chem. Phys.* **152** 084307
[12] Natan A, Schori A, Owolabi G, Cryan J P, Glownia J M and Bucksbaum P H 2021 *Faraday Discuss.* **228** 123–38
[13] Ruddock J M *et al* 2019 *Angew. Chem., Int. Ed.* **58** 6371–5
[14] Ruddock J M *et al* 2019 *Sci. Adv* **5** eaax6625
[15] Ware M R, Glownia J M, Al-Sayyad N, O'Neal J T and Bucksbaum P H 2019 *Phys. Rev.* A **100** 033413
[16] Bucksbaum P H, Ware M R, Natan A, Cryan J P and Glownia J M 2020 *Phys. Rev.* X **10** 011065
[17] Gabalski I *et al* 2022 *J. Chem. Phys.* **157** 164305
[18] Stankus B *et al* 2019 *Nat. Chem.* **11** 716–21
[19] Yong H *et al* 2021 *Proc. Natl Acad. Sci.* **118** e2021714118
[20] Yong H *et al* 2020 *Nat. Commun.* **11** 2157
[21] Pemberton C C, Zhang Y, Saita K, Kirrander A and Weber P M 2015 *J. Phys. Chem.* A **119** 8832
[22] Stankus B, Budarz J M, Kirrander A, Rogers D, Robinson J, Lane T J, Ratner D, Hastings J, Minitti M P and Weber P M 2016 *Faraday Discuss.* **194** 525–36
[23] Cao J and Wilson K R 1998 *J. Phys. Chem.* A **102** 9523
[24] Henriksen N E and Møller K B 2008 *J. Phys. Chem.* B **112** 558
[25] Lorenz U, Møller K B and Henriksen N E 2010 *Phys. Rev.* A **81** 023422
[26] Møller K B and Henriksen N E 2012 Time-resolved x-ray diffraction: The dynamics of the chemical bond *Molecular Electronic Structures of Transition Metal Complexes I* (*Structure and Bonding*) vol 142, ed Mingos D M P, Day P and Dahl J P (Springer) pp 185–211
[27] Dixit G, Vendrell O and Santra R 2012 *Proc. Natl Acad. Sci.* **109** 11636
[28] Dixit G and Santra R 2013 *J. Chem. Phys.* **138** 134311
[29] Kirrander A 2012 *J. Chem. Phys.* **137** 154310
[30] Suominen H J and Kirrander A 2014 *Phys. Rev. Lett.* **112** 043002
[31] Santra R, Dixit G and Slowik J M 2014 *Phys. Rev. Lett.* **113** 189301
[32] Kirrander A, Saita K and Shalashilin D V 2016 *J. Chem. Theory Comput.* **12** 957–67
[33] Tremblay J C, Pohl V, Hermann G and Dixit G 2021 *Faraday Discuss.* **228** 82–103
[34] Kirrander A and Weber P M 2017 *Appl. Sci.* **7** 534
[35] Simmermacher M, Henriksen N E and Møller K B 2017 *Phys. Chem. Chem. Phys.* **19** 19740–9
[36] Bennett K, Kowalewski M, Rouxel J R and Mukamel S 2018 *Proc. Natl Acad. Sci.* **115** 6538–47
[37] Simmermacher M, Henriksen N E, Møller K B, Moreno Carrascosa A and Kirrander A 2019 *Phys. Rev. Lett.* **122** 073003
[38] Simmermacher M, Henriksen N E, Møller K B, Moreno C A and Kirrander A 2019 *J. Chem. Phys.* **151** 174302
[39] Simmermacher M, Kirrander A and Henriksen N E 2020 *Phys. Rev.* A **102** 052825
[40] Hermann G, Pohl V, Dixit G and Tremblay J C 2020 *Phys. Rev. Lett.* **124** 013002
[41] Moreno Carrascosa A, Yang M, Yong H, Ma L, Kirrander A, Weber P M and Lopata K 2021 *Faraday Discuss.* **228** 60–81
[42] Ho P J, Fouda A E A, Li K, Doumy G and Young L 2021 *Faraday Discuss.* **228** 139–60
[43] Giri S, Tremblay J C and Dixit G 2021 *Phys. Rev.* A **104** 053115
[44] Yong H, Cavaletto S M and Mukamel S 2021 *J. Phys. Chem. Lett.* **12** 9800
[45] Yong H, Keefer D and Mukamel S 2022 *J. Am. Chem. Soc.* **144** 7796–804
[46] Ziems K M, Simmermacher M, Gräfe S and Kirrander A 2023 *J. Chem. Phys.* **159** 044108
[47] Ware M R, Glownia J M, Natan A, Cryan J P and Bucksbaum P H 2019 *Phil. Trans. R. Soc.* A **377** 20170477
[48] Yong H *et al* 2019 *J. Chem. Phys.* **151** 084301
[49] Zotev N, Carrascosa A M, Simmermacher M and Kirrander A 2020 *J. Chem. Theory Comput.* **16** 2594–605
[50] Yong H, Carrascosa A M, Ma L, Stankus B, Minitti M P, Kirrander A and Weber P M 2021 *Faraday Discuss.* **228** 104–22
[51] Acheson K and Kirrander A 2023 *J. Chem. Theory Comput.* **19** 2721–34
[52] Acheson K and Kirrander A 2023 *J. Chem. Theory Comput.* **19** 6126–38
[53] Hegazy K *et al* 2023 *Commun. Phys.* **6** 325
[54] Zholents A A and Fawley W M 2004 *Phys. Rev. Lett.* **92** 224801
[55] Prat E and Reiche S 2015 *Phys. Rev. Lett.* **114** 244801
[56] Hartmann N *et al* 2017 *Nat. Photon.* **12** 215–20
[57] Marinelli A, MacArthur J, Emma P, Guetg M, Field C, Kharakh D, Lutman A A, Ding Y and Huang Z 2017 *Appl. Phys. Lett.* **111** 151101
[58] Huang S, Ding Y, Feng Y, Hemsing E, Huang Z, Krzywinski J, Lutman A A, Marinelli A, Maxwell T J and Zhu D 2017 *Phys. Rev. Lett.* **119** 154801
[59] Duris J *et al* 2020 *Nat. Photon.* **14** 30–36
[60] Li S *et al* 2022 *Science* **375** 285–90
[61] Leone S R and Neumark D M 2016 *Faraday Discuss.* **194** 15–39
[62] Krausz F and Ivanov M 2009 *Rev. Mod. Phys.* **81** 163–234
[63] Merritt I C D, Jacquemin D and Vacher M 2021 *J. Phys. Chem. Lett.* **12** 8404–15
[64] Nobel Prize Outreach AB 2024 The Nobel Prize in Physics 2023 *nobelprize.org* (available at: www.nobelprize.org/prizes/physics/2023/summary/) (Accessed 11 June 2024)
[65] Simmermacher M, Weber P M and Kirrander A 2023 Theory of time-dependent scattering *Structural Dynamics With X-ray and Electron Scattering* (*Theoretical and Computational Chemistry Series* vol 25) 1st edn, ed K Amini, A Rouzée and M J J Vrakking (Royal Society of Chemistry) ch 3, p 85
[66] Makhija V, Veyrinas K, Boguslavskiy A E, Forbes R, Wilkinson I, Lausten R, Neville S P, Pratt S T, Schuurman M S and Stolow A 2020 *J. Phys. B: At. Mol. Opt. Phys.* **53** 114001
[67] Makhija V, Boguslavskiy A E, Forbes R, Veyrinas K, Wilkinson I, Lausten R, Schuurman M S, Grant E R and Stolow A 2021 *Faraday Discuss.* **228** 191–225
[68] Reuner M and Popova-Gorelova D 2023 *Phys. Rev.* A **107** 023101
[69] Keefer D, Aleotti F, Rouxel J R, Segatta F, Gu B, Nenov A, Garavelli M and Mukamel S 2021 *Proc. Natl Acad. Sci. USA* **118** e2022037118
[70] Kowalewski M, Bennett K and Mukamel S 2017 *Struct. Dyn.* **4** 054101
[71] Neville S P, Stolow A and Schuurman M S 2022 *J. Phys. B: At. Mol. Opt. Phys.* **55** 044004
[72] Robb M A 2014 In this molecule there must be a conical intersection *Advances in Physical Organic Chemistry* vol 48 (Elsevier) pp 189–228
[73] Pan S and Mies F H 1988 *J. Chem. Phys.* **89** 3096
[74] Donovan R J, Kirrander A and Lawley K P 2022 *Int. Rev. Phys. Chem.* **41** 97–175
[75] Reinhold E and Ubachs W 2002 *Phys. Rev. Lett.* **88** 013001
[76] Kirrander A 2010 *J. Chem. Phys.* **133** 121103
[77] Rose T S, Rosker M J and Zewail A H 1988 *J. Chem. Phys.* **88** 6672–3

[78] Rose T S, Rosker M J and Zewail A H 1989 *J. Chem. Phys.* **91** 7415–36
[79] Engel V and Metiu H 1989 *J. Chem. Phys.* **90** 6116–28
[80] Choi S E and Light J C 1989 *J. Chem. Phys.* **90** 2593–604
[81] Chapman S and Child M S 1991 *J. Phys. Chem.* **95** 578
[82] Dietz H and Engel V 1996 *Chem. Phys. Lett.* **255** 258–62
[83] Balakrishnan N, Esry B D, Sadeghpour H R, Cornett S T and Cavagnero M J 1999 *Phys. Rev.* A **60** 1407
[84] Tóth A, Csehi A, Halász G J and Vibók A 2019 *Phys. Rev.* A **99** 043424
[85] Cornett S T, Sadeghpour H R and Cavagnero M J 1999 *Phys. Rev. Lett.* **82** 2488
[86] Sadeghpour H R 2000 *Int. J. Quantum Chem.* **80** 958–65
[87] Mizunol Y and Hukushima K 2018 *J. Chem. Phys.* **149** 174313
[88] Betz V, Goddard B D and Manthe U 2016 *J. Chem. Phys.* **144** 224109
[89] Hosseini B H, Sadeghpour H R and Balakrishnan N 2005 *Phys. Rev.* A **71** 023402
[90] Shu C C and Henriksen N E 2011 *J. Chem. Phys.* **134** 164308
[91] Tóth A, Csehi A, Halász G J and Vibók A 2020 *Phys. Rev. Res.* **2** 013338
[92] Waller I and Hartree D R 1929 *Proc. R. Soc.* A **124** 119
[93] Debye P 1915 *Ann. Phys., NY* **46** 809
[94] Baskin J S and Zewail A H 2005 *ChemPhysChem* **6** 2261–76
[95] Baskin J S and Zewail A H 2006 *ChemPhysChem* **7** 1562–74
[96] Ho P J, Miller M R and Santra R 2009 *J. Chem. Phys.* **130** 154310
[97] Lorenz U, Møller K B and Henriksen N E 2010 *New J. Phys.* **12** 113022
[98] Stapelfeldt H and Seideman T 2003 *Rev. Mod. Phys.* **75** 543–57
[99] Werner H J, Knowles P J *et al* 2015 Molpro, version 2015.1, a package of ab initio programs (available at: www.molpro.net/)
[100] Varandas A J C 2009 *J. Chem. Phys.* **131** 124128
[101] Schmidt B and Lorenz U 2017 *Comput. Phys. Commun.* **213** 223–34
[102] The MathWorks Inc. 2021 MATLAB R2021b (available at: www.mathworks.com)
[103] Wang J and Smith J V H 1994 *Int. J. Quantum Chem.* **52** 1145–51
[104] Carrascosa A M, Yong H, Crittenden D L, Weber P M and Kirrander A 2019 *J. Chem. Theory Comput.* **15** 2836–46
[105] Moreno Carrascosa A, Coe J P, Simmermacher M, Paterson M J and Kirrander A 2022 *Phys. Chem. Chem. Phys.* **24** 24542–52
[106] Coe J P, Moreno Carrascosa A, Simmermacher M, Kirrander A and Paterson M J 2022 *J. Chem. Theory Comput.* **18** 6690–9
[107] Bewilogua L 1932 *Phys. Zeits.* **33** 688–92
[108] Prince E (ed) 2006 *International Tables for Crystallography, Volume C: Mathematical, Physical and Chemical Tables* 2006th edn (Wiley)
[109] Kirrander A, Jungen C and Fielding H H 2008 *J. Phys. B: At. Mol. Opt. Phys.* **41** 074022
[110] Kirrander A, Fielding H H and Jungen C 2010 *J. Chem. Phys.* **132** 024313
[111] Keefer D, Rouxel J R, Aleotti F, Segatta F, Garavelli M and Mukamel S 2021 *J. Am. Chem. Soc.* **143** 13806–15
[112] Yong H, Rouxel J R, Keefer D and Mukamel S 2022 *Phys. Rev. Lett.* **129** 103001